ARTICLE

High-Throughput and Label-Free Single Nanoparticle Sizing Based on Time-Resolved On-Chip Microscopy

Euan McLeod,*,†,‡ T. Umut Dincer,†,‡ Muhammed Veli,†,‡ Yavuz N. Ertas,‡ Chau Nguyen,§ Wei Luo,†,‡ Alon Greenbaum,†,‡ Alborz Feizi,‡ and Aydogan Ozcan*,†,‡,⊥,∥

†Electrical Engineering Department, University of California, Los Angeles, California 90095, United States, ‡Bioengineering Department, University of California, Los Angeles, California 90095, United States, §Chemistry & Biochemistry Department, University of California, Los Angeles, California 90095, United States, ⊥California NanoSystems Institute, University of California, Los Angeles, California 90095, United States, and ∥Department of Surgery, David Geffen School of Medicine, University of California, Los Angeles, California 90095, United States

ABSTRACT Sizing individual nanoparticles and dispersions of nanoparticles provides invaluable information in applications such as nanomaterial synthesis, air and water quality monitoring, virology, and medical diagnostics. Several conventional nanoparticle sizing approaches exist; however, there remains a lack of high-throughput approaches that are suitable for low-resource and field settings, *i.e.*, methods that are cost-effective, portable, and can measure widely varying particle sizes and concentrations. Here we fill this gap using an unconventional approach that combines holographic on-chip microscopy with vapor-condensed nanolens self-assembly inside a cost-effective hand-held device. By using this approach and capturing time-resolved *in situ* images of the particles, we optimize the nanolens formation process, resulting in significant signal enhancement for the label-free detection and sizing of individual deeply subwavelength particles (smaller than $\lambda/10$) over a 30 mm^2 sample field-of-view, with an accuracy of $\pm$11 nm. These time-resolved measurements are significantly more reliable than a single measurement at a given time, which was previously used only for nanoparticle detection without sizing. We experimentally demonstrate the sizing of individual nanoparticles as well as viruses, monodisperse samples, and complex polydisperse mixtures, where the sample concentrations can span ~5 orders-of-magnitude and particle sizes can range from 40 nm to millimeter-scale. We believe that this high-throughput and label-free nanoparticle sizing platform, together with its cost-effective and hand-held interface, will make highly advanced nanoscopic measurements readily accessible to researchers in developing countries and even to citizen-scientists, and might especially be valuable for environmental and biomedical applications as well as for higher education and training programs.

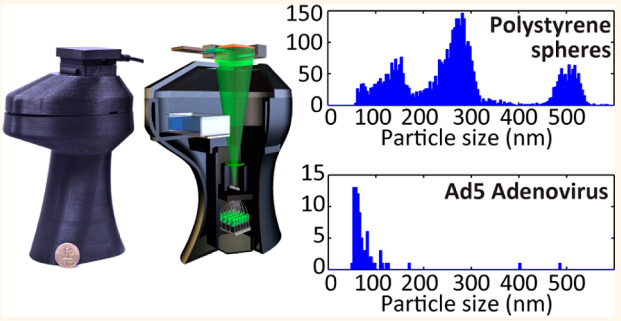

KEYWORDS: nanoparticles · particle-sizing · lensfree microscopy · field-portable

The ability to detect and size nanoparticles is extremely important in the analysis of liquid and aerosol samples for medical, biological, and environmental studies.[1−8] Some examples of nanoparticles that researchers have been interested in detecting and sizing include viruses,[9−11] exosomes,[1] metallic labels,[12,13] soot,[6,14] ice crystals in clouds,[15] and engineered nanomaterials,[16] among others. While there exist various nanoparticle detection and sizing methods, there is a lack of high-throughput instruments that can cover a large dynamic range of particle sizes and concentrations within a field-portable, cost-effective and rapid interface. Existing nonoptical methods, such as transmission electron microscopy (TEM), scanning electron microscopy (SEM), and atomic force microscopy, are typically very accurate and provide a gold standard for particle sizing;[1,4] however they are bulky, require significant capital investment, can be slow in image acquisition, and provide extremely restricted fields of view (FOVs) that limit throughput for particle sizing. Optical techniques can be more cost-effective and rapid; however, it is in general difficult to overcome the challenge of obtaining a large enough signal-to-noise (SNR) ratio to detect and reliably size both individual nanoparticles and populations of nanoparticles.

* Address correspondence to euanmc@ucla.edu, ozcan@ucla.edu.

Received for review January 18, 2015 and accepted February 17, 2015.

Published online February 17, 2015
10.1021/acsnano.5b00388

One way in which the challenge of low SNR has been mitigated is through the use of fluorescent labels,[1] although the (bio)chemistry of the detected particles must be known *a priori* so that they can be efficiently and specifically labeled with fluorophores or quantum dots. Fluorescent optical techniques include fluorescence correlation spectroscopy,[17] fluorescence flow cytometry,[18] and recently developed super-resolution techniques such as photoactivated localization microscopy (PALM), stochastic optical reconstruction microscopy (STORM),[19,20] and stimulated emission depletion (STED) microscopy.[21] Although these techniques can provide accurate sizing data, they too suffer from many of the drawbacks of the nonoptical methods: bulkiness, capital cost, relatively slow imaging speed as well as significantly restricted FOVs, which limit the sizing throughput.

Label-free nonfluorescent optical methods, on the other hand, have the advantage to quantify particle size distributions in chemically or biologically unknown heterogeneous samples. For particles in liquids, two common techniques are dynamic light scattering (DLS) and nanoparticle tracking analysis (NTA), both of which characterize suspensions of particles using Brownian motion. As it is a statistical method, DLS only provides collective sizing data about particles' hydrodynamic diameters, without providing sizing information on an individual particle-by-particle basis.[22] As a result of this, DLS has limited accuracy for polydisperse samples with size heterogeneity, and in particular has difficulty resolving bimodal (or multimodal) distributions where the modal means are either too closely spaced or too far apart.[23] In contrast, NTA tracks individual particles and can therefore better resolve different sizes in particle distributions.[24] However, both DLS and NTA tend to rely on bulky equipment, are limited in the range of particle concentrations they can handle (*e.g.*, too much dilution results in low signal, while high density results in high noise due to multiple scattering events), and require sufficiently small particles (less than a few microns in diameter) such that the Brownian motion is noticeable, which limits the dynamic range of particle sizes that can be probed with these techniques.

For aerosol measurements, several other label-free nonfluorescent nanoparticle sizing techniques are available, including differential mobility analysis, condensation particle counting, laser diffraction, and diffusion size classification. Laser diffraction simply observes the diffracted laser intensity of particles flowing through a chamber. However, because scattered intensity scales with the sixth power of a nanoparticle's diameter, it is difficult for this approach to detect particles smaller than ~100 nm.[25] A condensation particle counter enables detection of ultrasmall nanoparticles, and overcomes this challenge by using the particles of interest as nuclei for the condensation of a vapor around particles while they are still suspended in the gas flow.[26,27] This approach effectively increases the particles' sizes, making them easier to detect, although sizing accuracy may be compromised due to differing condensation rates around particles of different sizes. To provide higher sizing accuracy, laser diffraction and condensation particle counting can be combined with differential mobility analysis, which separates airborne particles based on size by first charging the particles, and then characterizing their mobility within an electric field. The resulting measurements depend on the electrical properties of the particles as well as their size. This technique exists in both large laboratory-based platforms, as well as relatively small platforms.[28,29]

For nanoparticle sizing measurements in either liquids or aerosols, holographic imaging provides an attractive label-free optical approach. Because holography captures particles' scattered fields through an interference pattern, measured signals scale with the *third* power of the of the particle diameter instead of the sixth power that is characteristic of the scattered intensity measurements discussed earlier. This endows holography with better signal scaling when detecting small particles.[30] Furthermore, holographic microscopy provides quantitative information on both particle amplitude (*e.g.*, absorption) as well as phase (*e.g.*, refractive index), which can be used in concert to improve sizing accuracy. Nonetheless, low SNR remains a challenge for detecting and sizing particularly small particles, and holographic imaging has historically been used for particle sizing at the microscale, generally in conjunction with large bulky laboratory equipment, such as laboratory grade optical microscopes with relatively expensive objective lenses.[8,15,31,32] On the other hand, in the *lensfree* holographic imaging platform developed in our group,[33,34] the sample of interest is placed on an optoelectronic sensor-array with typically less than 0.5 mm gap (z_2) between the sample and sensor planes such that, under unit magnification, the entire sensor active area serves as the imaging FOV, easily reaching >20−30 mm^2 with state-of-the-art CMOS imager chips. The initial sensitivity limit of this lensfree on-chip imaging approach has been ~200−300 nm; particles with diameters smaller than this are indistinguishable from background noise. Recently, we have shown different methods of generating self-assembled nanolenses that allow us to detect, using on-chip holographic imaging, particles as small as ~40 nm, *without* sizing capability.[9,30,35]

RESULTS AND DISCUSSION

Here we report the first demonstration of single nanoparticle sizing using on-chip microscopy, which is achieved through a holographic microscope design that incorporates tunable vapor condensation of nanolenses and time-resolved lensfree imaging in the same

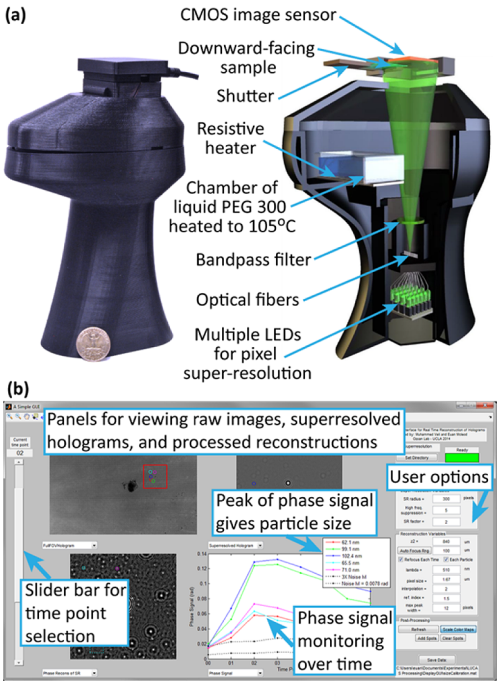

Figure 1. Nanoparticle sizing platform. (a) Physical hardware photograph and diagram. Imaging and vapor-condensed nanolens self-assembly are performed in a single hand-held device, which weighs less than 500 g. (b) Data analysis graphical user interface. Using this interface, users can measure the size of specific particles and monitor the signal enhancement provided by the self-assembled nanolenses.

hand-held device (Figure 1). Using this portable device and the reconstructed, time-resolved, and automatically focused phase images of the sample field-of-view, we quantified our sizing accuracy in both monodisperse and heterogeneous particle solutions, achieving an accuracy of ±11 nm for particles that range from 40 up to 500 nm. For larger particles, our technique still works while the accuracy roughly scales with particle size. As will be shown below, achieving this level of accuracy relies on the ability to image and time-resolve the nanolens deposition and growth *in situ*, which was not possible before this work. In addition, we have used this feature to verify our theoretical models for the vapor condensation rate, minimal energy nanolens shape evolution, and the impact of the growing nanolens on the holographic SNR. Compared to other nanoparticle sizing approaches in general, the lensfree holographic imaging and vapor condensation platform presented here provides highly advantageous features: label-free protocols, an ultralarge particle sizing range (~40 nm to millimeter-scale), an imaging-based approach that provides particle localization in addition to sizing information, field-portability, cost-effectiveness, and a large field of view that can handle a wide range of particle concentrations (spanning up to 6 orders of magnitude), as well as the potential to achieve spatially multiplexed detection and sizing of different target nanoparticles over a large area by patterning different capture zones.

The lensfree holographic imaging design (Figure 1) includes a 10 Mega-pixel complementary metal-oxide-semiconductor (CMOS) image sensor, a transparent sample substrate, an optical bandpass filter to provide partial temporal coherence, and 17 green light-emitting-diodes (LEDs) coupled to spatially separated multi-mode optical fibers, which provide sufficient spatial coherence at the sample plane for conducting in-line holographic imaging. These multiple LEDs are used to provide spatially shifted holograms, which can be synthesized into a single high-resolution hologram using a pixel super resolution technique.[36−39] The sample, a plasma-treated microscope cover glass with adsorbed nanoparticles of interest, is placed upside-down with the image sensor in direct contact with the back side of the sample. Using resolution test targets, we have verified that we can achieve deeply subpixel resolution and are able to routinely resolve grating patterns with submicron line-widths in this hand-held device, which weighs less than 500 g in total.

In addition to the imaging components, the other major custom-designed hardware in our platform is the vapor condensation system, which consists of a small resistive heater inside of a shallow glass dish, which rests to the side of the optical axis in a plastic housing fabricated *via* 3D printing. The glass dish is filled with polyethylene glycol (PEG, M_n = 300 Da). A physical shutter is included, which can isolate the sample from the vaporization chamber, if desired.

In a typical experiment, a set of low-resolution holograms will be acquired before any vapor condensation occurs in order to provide a baseline image. Particles that are smaller than several hundred nanometers are undetectable in each one of these lensfree images. The heater will then be activated and set to 105 °C using a feedback temperature controller. Higher temperatures can be used for faster operation, but with less precision in results. After the system reaches the set temperature (within ~4 min), another set of low-resolution lensfree holograms are acquired, with a period of, *e.g.*, 4 min. These sets of time-resolved lensfree holograms are much more reliable than a single lensfree measurement at a given time point, and enable us to accurately size a large range of particles with various compositions while also making our platform immune to experimental fluctuations in, *e.g.*, condensation rate, vapor density, *etc.* as will be detailed in our Results and Discussion Section.

During and after data acquisition, we use a custom-written graphical user interface for processing the acquired images (Figure 1b). This graphical interface processes and presents a large amount of information rapidly and in a convenient fashion, including the raw low-resolution holograms, high-resolution holograms synthesized using pixel super resolution, digitally reconstructed images of the sample, and time-traces of the signal from individual particles during the course of

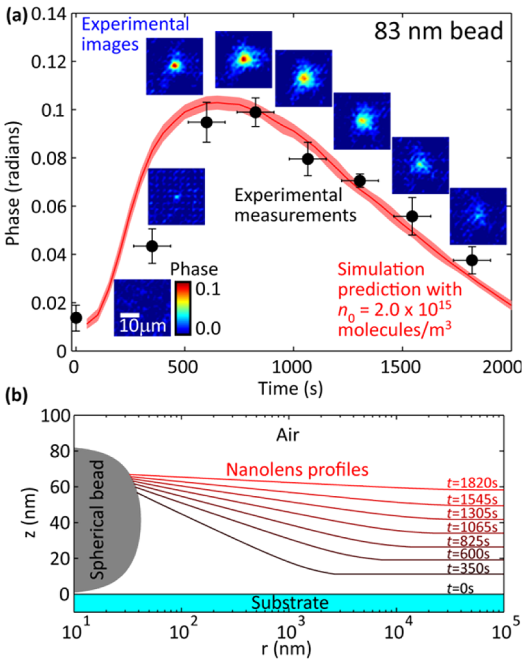

Figure 2. Nanolens formation and growth. (a) Comparison of experimental and simulated signals as a function of time for an 83 nm bead (illumination wavelength: 510 nm). Horizontal experimental error bars show the total time required to capture the set of low-resolution holograms that are used to synthesize a pixel super-resolved holographic image. Vertical experimental error bars have a length equal to twice the maximum difference in phase value between the brightest pixel and its four nearest neighbors for a given reconstructed lensfree particle image. The vertical span of the red curve depicts the standard deviation of eight simulations run with different random noise. (b) Simulated nanolens shape at the experimental time points from (a).

the experiment. The same interface also automatically compensates for possible mechanical drifts in *x*, *y*, and *z* of the sample between different time points. As we are using a digital holographic approach, both amplitude images (similar to brightfield) and phase images (similar to phase contrast) are available after digital reconstruction.[40] For the nanolens-nanoparticle complexes studied here, we find the phase images to be more sensitive and we use this information channel to define the "signal" of the particles we image and quantify, which will be detailed and discussed in the next section.

During the course of each experiment, PEG evaporates from its reservoir due to its elevated temperature. Some of this PEG vapor then condenses on the cooler sample surface. As the PEG condenses on the sample, it forms a continuous film that thickens over time. In the vicinity of nanoparticles adsorbed on the substrate, this continuous film rises in the form of a meniscus that acts as a nanolens that increases the scattering from the particle and helps to direct light toward the image sensor, thereby boosting the particle's heterodyne holographic signature (Figure 2). This increase in holographic signature enables the detection of ultrasmall subwavelength particles that could not be detected in this platform without the use of the vapor-condensed film, such as the 83 nm particle example shown in Figure 2, whose size was verified using SEM. After sufficient vapor condensation, the PEG film becomes so thick that it begins to bury the nanoparticle under a thick layer, resulting in a loss of signal at late times. In Figure 2, we see this behavior in both the experimental results (filled black circles and accompanying reconstructed lensfree images), as well as the simulated results (red). These simulations include 1% random white Gaussian noise added at the sensor (hologram) plane, which generates the small spread in simulation results whose span is indicated by the red shaded region. These simulation results depend on a *single* fitting parameter, *the vapor density*, which is here assumed to be 2.0 $\times$ 10^{15} molecules/m^3.[30] With this single fitting parameter, we find good agreement between our simulations and the experimental results for this 83 nm bead. The simulations used here incorporate physical modeling of the shape of the nanolens as a function of time (Figure 2b), as well as optical simulations of the hologram formation and reconstruction process.[9,30] Beyond verifying our simulations, we also use these time-resolved lensfree measurements to identify and record the maximum signal obtained over the course of the experiment, which correlates strongly with particle size as will be detailed below. Therefore, time-resolving the optimum phase signal value instead of the signal value at a specific fixed time point maximizes the sensitivity of our approach to small particles and improves sizing accuracy by making the procedure robust to variable heating temperatures and unknown vapor densities.

In Figure 3, we have repeated the same analysis shown in Figure 2 for 121 other spherical particles in order to test the repeatability and accuracy of our sizing platform. Figure 3 plots the time-resolved maximum phase signal (*e.g.*, the phase value of the uppermost black circle in Figure 2a) as a function of the true particle size, which was measured using SEM. The points plotted here are drawn from 5 different experiments each with mixtures of bead sizes and 16−32 beads per experiment, where the throughput in this specific case has been limited by the process of acquiring SEM comparison images. The experiments had overlapping size ranges to ensure repeatability between experiments as well as consistency among beads within a single experiment. We find our limit in smallest detectable particle size to be approximately 40 nm, which very well coincides with 3 times the typical background noise (standard deviation of the pixels in a region without any particles), which is of order 0.01 radians.

The red curve in Figure 3a shows the simulated prediction for the reconstructed peak phases of detected particles based on modeling of the vapor-condensed nanolens shape and its influence on optical

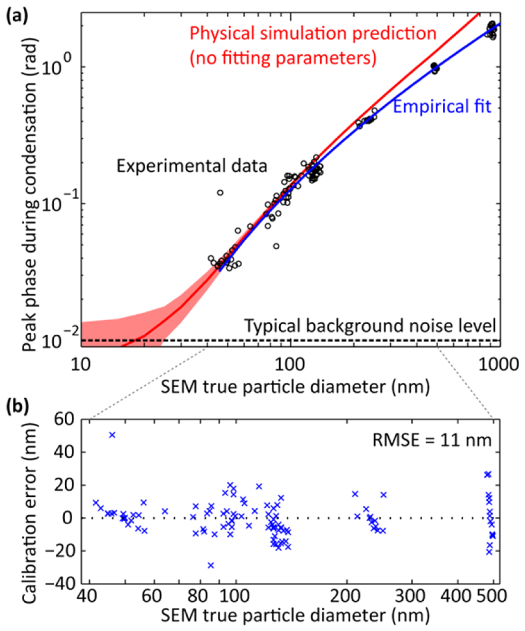

Figure 3. Sizing calibration curve and precision. (a) Reconstructed peak phase as a function of true particle diameter measured using SEM. Experimental measurements from 122 beads are shown (black circles), along with simulation predictions (red) based on our theoretical model, and an empirical fit (blue) that is used to calibrate the system for particle sizing. (b) Calibration error in particle sizing given by the horizontal difference between the true particle diameter and the blue empirical curve in (a). For nanoparticles in the 40−500 nm range, the root-mean-square-error (RMSE) is 11 nm.

scattering. It is important to note that this curve involves *no fitting parameters*, as the peak phase value is independent of the PEG vapor density (although the time at which this peak signal is achieved is dependent on the vapor density); this is an important example of how time-resolved holographic imaging significantly improves our detection sensitivity while also making our measurements more repeatable and robust to experimental factors. The shaded region encompassing the red line shows the standard deviation in the spread of eight different simulation results using different random noise fields added at the sensor plane. The good agreement between our experimental results and this physical model (without any fitting parameters) also illustrates the success of our theoretical modeling and understanding of the mechanisms behind the contrast enhancement provided by the vapor-condensed nanolenses. For particles larger than several hundred nanometers, we notice a small divergence between our simulation predictions and the experimental results. This divergence can be a result of our thin-lens approximation used to model the nanoparticle-nanolens system, which works well for small particles, but not as well for larger particles.

While the red curve demonstrates our physical modeling of the system, the blue curve in Figure 3a is the more practically useful calibration curve for evaluating this system as a particle sizing platform. This blue curve is an empirical second order polynomial fit (in log-space) to the experimental data, and it serves as a calibration curve for the platform that provides the best one-to-one relationship between the measured peak phase and the true particle diameter. The sizing error between the experimental data and the true particle size is shown in Figure 3b. For particles between 40 and 500 nm, the root-mean-square error is ±11 nm, which is relatively independent of particle size, indicating that it is better to characterize the error as an absolute error rather than a relative (percentage) error in this size range.

With the calibration curve determined, we have then applied this platform to blind sizing of large numbers of nanoparticles. In Figure 4, histogram sizing results from several types of samples are shown, including monodisperse polymer nanospheres (Figure 4a,b), polydisperse polymer nanospheres (Figure 4c,d), nonspherical inorganic particles (Figure 4e), and viruses (Figure 4f). Figure 4a depicts the sizing of 50 nm particles, which are close to our minimum measurable size. Figure 4b shows the measurement results from a dense sample of 100 nm beads, where more than 32 000 beads were measured. Due to the density of the sample, a secondary peak corresponding to particle clusters is also observed. We estimate that we can detect particle surface densities in excess of 1 particle per $(5\ \mu m)^2$, enabling imaging and sizing of more than 10^6 particles across the full 30 mm^2 active area of the sensor-array, although clusters will also be present. Figure 4c and 4d demonstrate that using the presented computational lensfree on-chip imaging approach, it is possible to accurately size heterogeneous nanoparticle populations that are typically very challenging for even benchtop DLS instruments.

The gadolinium-silica core−shell nanocrescent moon shape particle in Figure 4e is another example of a sample that is very challenging for DLS due to the nonspherical nature of these particles. These nanocrescents are expected to find uses as high contrast magnetic resonance imaging agents. For this sample, manual TEM sizing (see the inset in Figure 4e) showed that the particle diameters ranged from 120 to 200 nm. Our results show many particles in this range, but we also measure some particles smaller than 120 nm. We partially attribute this discrepancy to our use of a spherical bead calibration curve to size nonspherical particles. While these particles' true diameters are in the range 120−200 nm, their *true heights* (chords) are typically much smaller (~50 nm). Therefore, we would expect these nonstandard half-shell particles to be sized similar to nanospheres with diameters somewhere between 50 and 200 nm, depending on the orientation of the individual particle with respect to the substrate, along with its size. Although the nanolens-based sizing approach used here is more sensitive to the height of the nanoparticle and therefore is not as

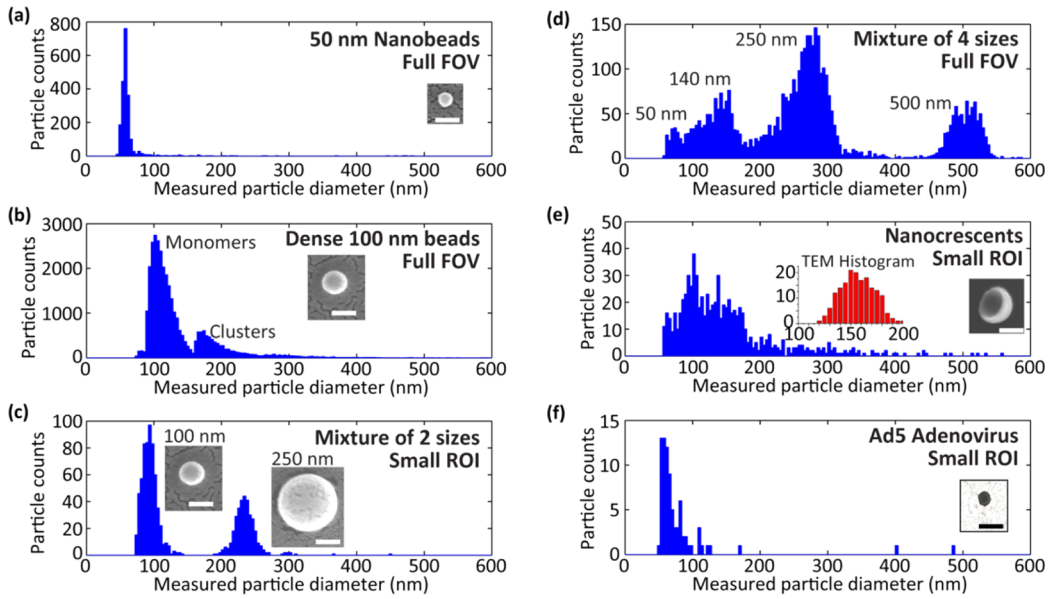

Figure 4. Blind nanoparticle sizing histograms. Sizing results of (a) 50 nm polystyrene beads, (b) 100 nm polystyrene beads, (c) a mixture of 100 and 250 nm polystyrene beads, (d) a mixture of 50, 140, 250, and 500 nm polystyrene beads, (e) gadolinium-silica nanocrescents (see text for related discussion), and (f) Ad5 adenovirus particles, whose sizes range from 50 to 80 nm.[41−43] Insets show electron microscope images of typical particles. Inset in (f) is reproduced from ref 41. All scale bars are 100 nm. Histogram inset in (e) is the result of manual TEM measurements of the longest nanocrescent dimension. On the basis of our own SEM measurements, the mean sizes, standard errors of the mean, and standard deviation of the bead populations are as follows. 50 nm: mean = 49 ± 1.1 nm, σ = 4.3 nm. 100 nm: mean = 101 ± 2.6 nm, σ = 9.4 nm. 140 nm: mean = 129 ± 0.8 nm, σ = 4.1 nm. 250 nm: mean = 234 ± 3.7 nm, σ = 12.7 nm. 500 nm: mean = 489 ± 1.4 nm, σ = 5.3 nm.

accurate as TEM for these nonspherical particles, it still remains very useful for approximate sizing and particle distribution measurements, significantly out-performing the capabilities of traditional DLS techniques.

Next, Figure 4f demonstrates the applicability of this technique to the sizing of biological particles, where we have successfully sized Ad5 adenoviruses, whose typical sizes range from 50 to 80 nm.[41−43] These viral particle sizing measurements could be potentially useful for viral load monitoring in resource limited settings or for quality control in the culturing and purification of viruses for, *e.g.*, vaccine and antiviral drug development efforts.

To generate the histograms in Figure 4, we have developed an automated segmentation algorithm (Figure 5) to localize and size particles based on lensfree phase image reconstructions. The approach here was custom-developed in order to correctly identify and size very small particles, which in some cases generated signals that were very similar to twin-image noise[33] that was present around larger particles or to random background noise. In addition to Figures 5 and 6, this procedure is also depicted in Movie S1 (Supporting Information). The algorithm begins by computing a super-resolved hologram from a set of low-resolution raw images.[39] This pixel super-resolved hologram is then back-propagated to multiple z_2 distances to generate the phase image reconstructions in the vicinity of the object plane. From this reconstruction we first count the largest objects, which have a peak phase value greater than a specific threshold (see the Methods section for details). After counting these larger particles, their associated twin image noise artifacts are digitally removed one by one. Then we reduce the phase threshold value and count the particles that are slightly smaller. This iterative count-and-clean procedure (also see Movie S1) is repeated five times, until the smallest particles (those with diameter ~40−50 nm) are counted.

The benefits of this iterative count-and-clean algorithm can be seen in Figure 6a and 6b, where 56 and 40 nm particles that were initially buried in the twin image noise of a larger (~590 nm) particle become clearly visible after the larger particle has been counted and its signature digitally removed from the lensfree image. To find the peak phase as a function of time (*e.g.*, Figure 2), which is correlated with the particle size (Figure 3), we repeat this analysis over all the time-resolved lensfree images. We then merge the peak phase data so that for each spot, we only keep the largest peak phase found out of all the z_2 and time values. Through our calibration experiments, we found that there are often a number of false positives, *i.e.*, particle-like noisy features that appear in our reconstructed phase images, especially when imaging <70 nm particles. To be able to automatically reject such spurious nonphysical features and therefore significantly reduce our false characterization rate, we apply an additional focusing criterion to separate physical particles from random noise: for each spot of interest that falls within our dynamic phase threshold value for particle sizing, plotting the phase as a

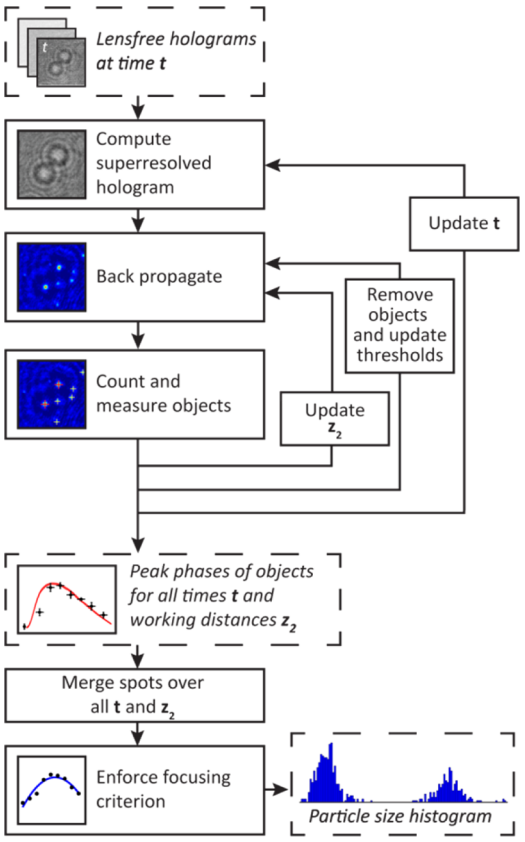

Figure 5. Automated nanoparticle sizing algorithm. For each particle image that is reconstructed using a lensfree hologram, we find its peak phase value by digitally optimizing the reconstructed working distance z_2, and the measurement time t. An iterative procedure (which we term count-and-clean) is used that progressively counts and then removes larger objects before attempting to detect and size smaller objects. This process prevents holographic twin image noise associated with larger particles from being counted as extraneous smaller particles.

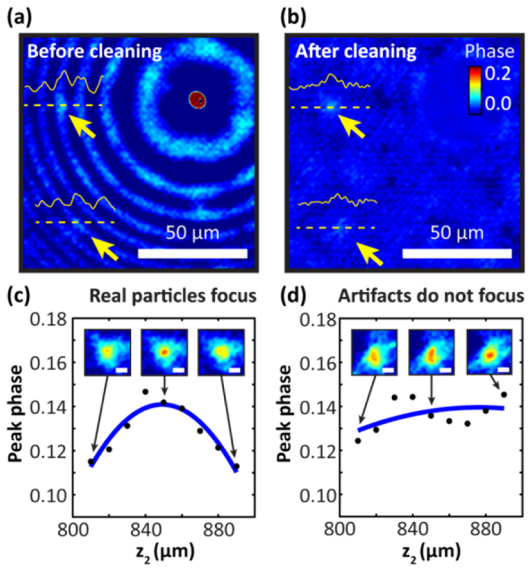

Figure 6. Effects of count-and-clean algorithm and the depth focusing criterion. (a) Phase reconstruction before the iterative count-and-clean procedure. A large particle is visible at the top-right with significant holographic twin-image noise. (b) Phase reconstruction after 4 iterations of the count-and-clean procedure. Two smaller particles that were previously buried in the twin image noise are now clearly visible. (c) A true particle comes into focus at an optimal z_2 value. (d) Spurious particle-like features do not exhibit a clear optimum reconstruction z_2, even though reconstruction images at specific z_2 values individually look very similar to those in (c).

function of reconstruction depth (z_2) must show a clear peak, indicating that the particle comes into focus at a plausible z_2. Figure 6c and 6d show an example of a particle that focuses well and an example of a spurious particle-like feature that does not focus well, respectively. After this additional "focusing criterion" is applied, the aggregate set of peak phases that show focusing behavior are converted to particle sizes using the calibration curve from Figure 3, and are plotted as histograms (*e.g.*, Figure 4). This automated particle detection algorithm is capable of accurately identifying particles larger than ~50 nm, making it slightly less sensitive than a human observer operating the graphical user interface program (Figure 1b), where we can achieve reliable detection of individual nanoparticles relative to background noise down to ~40 nm, which also coincides with 3 times the typical background noise in our phase reconstruction images.

In summary, we have demonstrated the fully functional prototype of a high-throughput and label-free nanoparticle sizing platform capable of sizing individual nanoparticles as small as ~40 nm with an accuracy of ±11 nm using self-assembled nanolenses and on-chip microscopy, all in a portable and cost-effective instrument. This platform includes the necessary hardware for vaporizing PEG and time-resolved imaging of nanoparticle samples, along with the necessary software for controlling the nanolens formation and imaging sequence, and for automated processing of the resulting data cube. We hope that this platform will provide an alternative to electron microscopy in resource-limited settings (at least for particle detection and sizing needs), as well as an alternative to dynamic light scattering and other optical sizing methods when location-specific sizing distribution is required of individual nanoparticles in a complex heterogeneous sample.

METHODS

Sample Preparation. The nanoparticle sample of interest is suspended in water. A glass coverslip (size 22 × 22 mm, thickness ~150 μm) is used as a substrate. This coverslip is plasma treated using a hand-held plasma generator (Electro-Technic Products, BD-10AS) for 30 s to ensure the substrate is hydrophilic. A small drop (3−7 μL) of the nanoparticle suspension is deposited on one side of the glass coverslip, and left to

rest for between 1 and 5 min. After resting, the sample is lightly rinsed with pure deionized (DI) water to remove any salts or surfactants that may have been present in the stock nanoparticle solutions. During this light rinsing procedure, many nanoparticles remain stuck to the substrate and are not washed away. If left to evaporate without rinsing, dissolved salts can form nanoscopic crystals that appear as impurities in the sizing distributions.

Sample Imaging and Nanolens Deposition. The imaging system consists of a portable pixel-super-resolution light source,[39] an optical bandpass filter (510 nm center wavelength with 10 nm bandwidth), the transparent sample to be imaged, and a 10 megapixel, 1.67 μm pixel size, CMOS image sensor with USB readout board (Imaging Development Systems UI-1492LE-M). The sample is placed in contact with the CMOS image sensor, where the side with adsorbed nanoparticles is facing away from the sensor chip. The distance between the particles and the active area of the sensor is ~0.9 mm, including both the cover glass thickness and the thickness of the sensor's protective glass. The imaging system is controlled using a custom-written LabVIEW program.

The nanolens deposition system consists of a reservoir of liquid PEG of molecular weight 300 Da (Sigma-Aldrich, 202371), a small resistive heater submersed within the PEG reservoir for evaporating the PEG (Omega Engineering, KHLV-101/10), a computer-controlled feedback temperature controller with thermistor immersed in the PEG used to heat it to a desired temperature (TE Technology, Inc. TC-48−20), and a shutter that can be used to shield the sample from PEG vapor, as desired. The temperature is set and maintained using a LabVIEW program.

The device is operated by first capturing a set of images before condensation to provide a baseline signal. The temperature controller is then activated, with a heating set point of 105 °C. During the condensation procedure, lensfree images are acquired. The super-resolution imaging system captures 20 lensfree holograms for each measurement. Capturing these 20 images takes approximately 3.5 min, which can be significantly improved with different frame-grabber hardware systems. Every 4 min, a new measurement is performed and a new set of lensfree images captured. The evolution of the sample and condensing PEG nanolenses are thus recorded throughout the duration of the experiment.

Data Processing. Please see Supporting Information for these methods.

Conflict of Interest: The authors declare the following competing financial interest(s): A.O. is the founder of a company that commercializes computational imaging and diagnostics technologies.

Acknowledgment. The Ozcan Research Group at UCLA gratefully acknowledges the support of the Presidential Early Career Award for Scientists and Engineers (PECASE), Army Research Office (ARO) Life Sciences Division (ARO; W911NF-13-1-0419 and W911NF-13-1-0197), ARO Young Investigator Award, National Science Foundation (NSF) CAREER Award, NSF CBET Division Biophotonics Program, NSF Emerging Frontiers in Research and Innovation (EFRI) Award, NSF EAGER Award, NSF INSPIRE Award, Office of Naval Research (ONR), the Howard Hughes Medical Institute (HHMI), and National Institutes of Health (NIH) Director's New Innovator Award DP2OD006427 from the Office of the Director, National Institutes of Health. This work is partially based upon research performed in a renovated laboratory by the National Science Foundation under Grant No. 0963183, which is an award funded under the American Recovery and Reinvestment Act of 2009 (ARRA). The authors also acknowledge Najva Akbari of UCLA for help in the assembly of the imaging light source, Derek Tseng of UCLA for help in the production of artwork and three-dimensional CAD images, and Haydar Ozkan, Faizan Shabbir, and Steve Feng for helpful discussions regarding automated data processing.

Supporting Information Available: Supplementary data processing methods including the data processing and analysis of single particles as well as automated histogram generation. This material is available free of charge *via* the Internet at http://pubs.acs.org.

REFERENCES AND NOTES

1. Van Der Pol, E.; Hoekstra, A. G.; Sturk, A.; Otto, C.; Van Leeuwen, T. G.; Nieuwland, R. Optical and Non-Optical Methods for Detection and Characterization of Microparticles and Exosomes. *J. Thromb. Haemostasis* **2010**, *8*, 2596–2607.
2. Canton, I.; Battaglia, G. Endocytosis at the Nanoscale. *Chem. Soc. Rev.* **2012**, *41*, 2718–2739.
3. Biswas, P.; Wu, C.-Y. Nanoparticles and the Environment. *J. Air Waste Manage. Assoc.* **2005**, *55*, 708–746.
4. Paterson, G.; Macken, A.; Thomas, K. V. The Need for Standardized Methods and Environmental Monitoring Programs for Anthropogenic Nanoparticles. *Anal. Methods* **2011**, *3*, 1461–1467.
5. Domingos, R. F.; Baalousha, M. A.; Ju-Nam, Y.; Reid, M. M.; Tufenkji, N.; Lead, J. R.; Leppard, G. G.; Wilkinson, K. J. Characterizing Manufactured Nanoparticles in the Environment: Multimethod Determination of Particle Sizes. *Environ. Sci. Technol.* **2009**, *43*, 7277–7284.
6. Long, C. M.; Nascarella, M. A.; Valberg, P. A. Carbon Black *vs.* Black Carbon and Other Airborne Materials Containing Elemental Carbon: Physical and Chemical Distinctions. *Environ. Pollut.* **2013**, *181*, 271–286.
7. Lam, C.; James, J. T.; McCluskey, R.; Arepalli, S.; Hunter, R. L. A Review of Carbon Nanotube Toxicity and Assessment of Potential Occupational and Environmental Health Risks. *Crit. Rev. Toxicol.* **2006**, *36*, 189–217.
8. Berg, M. J.; Subedi, N. R. Holographic Interferometry for Aerosol Particle Characterization. *J. Quant. Spectrosc. Radiat. Transfer* **2015**, *150*, 36–41.
9. Mudanyali, O.; McLeod, E.; Luo, W.; Greenbaum, A.; Coskun, A. F.; Hennequin, Y.; Allier, C. P.; Ozcan, A. Wide-Field Optical Detection of Nanoparticles Using on-Chip Microscopy and Self-Assembled Nanolenses. *Nat. Photonics* **2013**, *7*, 247–254.
10. Wei, Q.; Qi, H.; Luo, W.; Tseng, D.; Ki, S. J.; Wan, Z.; Göröcs, Z.; Bentolila, L. A.; Wu, T.-T.; Sun, R.; *et al.* Fluorescent Imaging of Single Nanoparticles and Viruses on a Smart Phone. *ACS Nano* **2013**, *7*, 9147–9155.
11. Inci, F.; Tokel, O.; Wang, S.; Gurkan, U. A.; Tasoglu, S.; Kuritzkes, D. R.; Demirci, U. Nanoplasmonic Quantitative Detection of Intact Viruses from Unprocessed Whole Blood. *ACS Nano* **2013**, *7*, 4733–4745.
12. Monroe, M. R.; Daaboul, G. G.; Tuysuzoglu, A.; Lopez, C. A.; Little, F. F.; Unlü, M. S. Single Nanoparticle Detection for Multiplexed Protein Diagnostics with Attomolar Sensitivity in Serum and Unprocessed Whole Blood. *Anal. Chem.* **2013**, *85*, 3698–3706.
13. Wei, Q.; McLeod, E.; Qi, H.; Wan, Z.; Sun, R.; Ozcan, A. On-Chip Cytometry Using Plasmonic Nanoparticle Enhanced Lensfree Holography. *Sci. Rep.* **2013**, *3*, 1699.
14. Kittelson, D. B. Engines and Nanoparticles: A Review. *J. Aerosol Sci.* **1998**, *29*, 575–588.
15. Fugal, J. P.; Shaw, R. A. Cloud Particle Size Distributions Measured with an Airborne Digital in-Line Holographic Instrument. *Atmos. Meas. Tech.* **2009**, *2*, 259–271.
16. Ertas, Y. N.; Jarenwattananon, N. N.; Bouchard, L.-S. Gadolinium Nanocrystals with Large Magnetic Moments for Applications in Biomolecular Imaging. *Adv. Mater.* **2014**submitted.
17. Starchev, K.; Buffle, J.; Pérez, E. Applications of Fluorescence Correlation Spectroscopy: Polydispersity Measurements. *J. Colloid Interface Sci.* **1999**, *213*, 479–487.
18. Perez-Pujol, S.; Marker, P. H.; Key, N. S. Platelet Microparticles Are Heterogeneous and Highly Dependent on the Activation Mechanism: Studies Using a New Digital Flow Cytometer. *Cytometry, Part A* **2007**, *71A*, 38–45.
19. Rust, M. J.; Bates, M.; Zhuang, X. Sub-Diffraction-Limit Imaging by Stochastic Optical Reconstruction Microscopy (STORM). *Nat. Methods* **2006**, *3*, 793–796.

20. Betzig, E.; Patterson, G. H.; Sougrat, R.; Lindwasser, O. W.; Olenych, S.; Bonifacino, J. S.; Davidson, M. W.; Lippincott-Schwartz, J.; Hess, H. F. Imaging Intracellular Fluorescent Proteins at Nanometer Resolution. *Science* **2006**, *313*, 1642–1645.
21. Hell, S. W. Far-Field Optical Nanoscopy. *Science* **2007**, *316*, 1153–1158.
22. Berne, B. J.; Pecora, R. *Dynamic Light Scattering: With Applications to Chemistry, Biology, and Physics*; Courier Dover Publications: Mineola, NY, 2000.
23. Filella, M.; Zhang, J.; Newman, M. E.; Buffle, J. Analytical Applications of Photon Correlation Spectroscopy for Size Distribution Measurements of Natural Colloidal Suspensions: Capabilities and Limitations. *Colloids Surf., A* **1997**, *120*, 27–46.
24. Filipe, V.; Hawe, A.; Jiskoot, W. Critical Evaluation of Nanoparticle Tracking Analysis (NTA) by NanoSight for the Measurement of Nanoparticles and Protein Aggregates. *Pharm. Res.* **2010**, *27*, 796–810.
25. Measurement of particle size distributions http://www.malvern.com/en/products/measurement-type/particle-size/default.aspx (accessed Oct 4, 2014).
26. Kulkarni, P.; Baron, P. A.; Willeke, K. *Aerosol Measurement: Principles, Techniques, and Applications*; John Wiley & Sons: New York, 2011.
27. Iida, K.; Stolzenburg, M. R.; McMurry, P. H. Effect of Working Fluid on Sub-2 nm Particle Detection with a Laminar Flow Ultrafine Condensation Particle Counter. *Aerosol Sci. Technol.* **2009**, *43*, 81–96.
28. Scanning Mobility Particle Sizer Spectrometers http://www.tsi.com/Scanning-Mobility-Particle-Sizer-Spectrometers/ (accessed Oct 4, 2014).
29. Matter Aerosol - DiSCmini - Handheld nano particle counter http://www.matter-aerosol.ch/index.php/features/jquery-superfish-menu (accessed Oct 4, 2014).
30. McLeod, E.; Nguyen, C.; Huang, P.; Luo, W.; Veli, M.; Ozcan, A. Tunable Vapor-Condensed Nanolenses. *ACS Nano* **2014**, *8*, 7340–7349.
31. Berg, M. J.; Videen, G. Digital Holographic Imaging of Aerosol Particles in Flight. *J. Quant. Spectrosc. Radiat. Transfer* **2011**, *112*, 1776–1783.
32. Seifi, M.; Fournier, C.; Grosjean, N.; Méès, L.; Marié, J.-L.; Denis, L. Accurate 3D Tracking and Size Measurement of Evaporating Droplets Using in-Line Digital Holography and "Inverse Problems" Reconstruction Approach. *Opt. Express* **2013**, *21*, 27964–27980.
33. Mudanyali, O.; Tseng, D.; Oh, C.; Isikman, S. O.; Sencan, I.; Bishara, W.; Oztoprak, C.; Seo, S.; Khademhosseini, B.; Ozcan, A. Compact, Light-Weight and Cost-Effective Microscope Based on Lensless Incoherent Holography for Telemedicine Applications. *Lab. Chip* **2010**, *10*, 1417.
34. Greenbaum, A.; Luo, W.; Su, T.-W.; Göröcs, Z.; Xue, L.; Isikman, S. O.; Coskun, A. F.; Mudanyali, O.; Ozcan, A. Imaging without Lenses: Achievements and Remaining Challenges of Wide-Field on-Chip Microscopy. *Nat. Methods* **2012**, *9*, 889–895.
35. Hennequin, Y.; Allier, C. P.; McLeod, E.; Mudanyali, O.; Migliozzi, D.; Ozcan, A.; Dinten, J.-M. Optical Detection and Sizing of Single Nanoparticles Using Continuous Wetting Films. *ACS Nano* **2013**, *7*, 7601–7609.
36. Hardie, R. C. High-Resolution Image Reconstruction from a Sequence of Rotated and Translated Frames and Its Application to an Infrared Imaging System. *Opt. Eng.* **1998**, *37*, 247.
37. Elad, M.; Hel-Or, Y. A Fast Super-Resolution Reconstruction Algorithm for Pure Translational Motion and Common Space-Invariant Blur. *IEEE Trans. Image Process.* **2001**, *10*, 1187–1193.
38. Bishara, W.; Su, T.-W.; Coskun, A. F.; Ozcan, A. Lensfree on-Chip Microscopy over a Wide Field-of-View Using Pixel Super-Resolution. *Opt. Express* **2010**, *18*, 11181–11191.
39. Greenbaum, A.; Akbari, N.; Feizi, A.; Luo, W.; Ozcan, A. Field-Portable Pixel Super-Resolution Colour Microscope. *PLoS One* **2013**, *8*, e76475.
40. Gorocs, Z.; Ozcan, A. On-Chip Biomedical Imaging. *IEEE Rev. Biomed. Eng.* **2013**, *6*, 29–46.
41. Alba, R.; Cots, D.; Ostapchuk, P.; Bosch, A.; Hearing, P.; Chillon, M. Altering the Ad5 Packaging Domain Affects the Maturation of the Ad Particles. *PLoS One* **2011**, *6*, e19564.
42. Ugai, H.; Dobbins, G. C.; Wang, M.; Le, L. P.; Matthews, D. A.; Curiel, D. T. Adenoviral Protein V Promotes a Process of Viral Assembly through Nucleophosmin 1. *Virology* **2012**, *432*, 283–295.
43. Zeng, Q.; Han, J.; Zhao, D.; Gong, T.; Zhang, Z.; Sun, X. Protection of Adenovirus from Neutralizing Antibody by Cationic PEG Derivative Ionically Linked to Adenovirus. *Int. J. Nanomed.* **2012**, *7*, 985–997.